

Exploring Thermoset Fracture with A Quantum Chemically Accurate Model of Bond Scission

¹

Zheng Yu and Nicholas E. Jackson*

*Department of Chemistry, University of Illinois at Urbana-Champaign, Urbana, Illinois, 61801,
USA*

E-mail: jacksonn@illinois.edu

²

Abstract

A molecular understanding of thermoset fracture is crucial for enhancing performance and durability across applications. However, achieving accurate atomistic modeling of thermoset fracture remains computationally prohibitive due to the high cost associated with quantum mechanical methods for describing bond breaking. In this work, we introduce an active learning (AL) framework for our recently developed machine-learning based adaptable bond topology (MLABT) model that uses datasets generated via density functional theory (DFT) calculations that are both minimalistic and informative. Employing MLABT integrated with AL and DFT, we explore fracture behavior in highly crosslinked thermosets, assessing the variations in fracture behavior induced by system temperature, temperature fluctuations, strain rate, cooling rate, and degree of crosslinking. Notably, we discover that while fracture is minimally affected by temperature, it is strongly influenced by strain rate. Furthermore, while the structural disparities introduced by different network annealing rates influence the elastic properties, they are inconsequential for thermoset fracture. In contrast, network topology emerges as the dominant determinant of fracture, influencing both the ultimate strain and stress. Particularly,

17 MLABT with AL-DFT achieving near quantum-chemical accuracy in bond breaking still leads
18 to ductile failures, emphasizing the necessity of modeling polymer networks at larger length
19 scales for bridging the gap between experiment and simulation. Nevertheless, the integration
20 of MLABT with the AL framework paves the way for efficient and DFT-accurate modeling
21 of thermoset fracture, providing an affordable and accurate approach for calculating polymer
22 network fracture across chemical space.

23 **Introduction**

24 Thermosets, characterized by the presence of irreversible polymer crosslinks and enhanced me-
25 chanical properties, are foundational to numerous technological applications ranging from auto-
26 motive components and aerospace structures to medical devices and protective coatings.¹⁻³ The
27 robust nature of thermosets along with their adaptability have ushered in new horizons for mate-
28 rial innovations.^{4,5} Central to maximizing the potential of thermosets in these domains is an in-
29 depth understanding of their fracture behaviors.⁶⁻¹⁰ Recent advancements in computational tools
30 and experimental techniques have provided insights into the fracture of thermosets.¹¹⁻¹⁸ How-
31 ever, the atomic-scale processes governing these behaviors remain less explored. Delving into
32 this atomic realm promises not only enhanced material predictability but also the prospect of tai-
33 lored design.^{19,20} Nevertheless, this pursuit presents formidable challenges: accurate atomic-level
34 modeling of thermoset fracture necessitates substantial computational resources, especially when
35 elucidating intricate bond breakage phenomena with quantum mechanical (QM) methods.²¹ As
36 the demand for higher performance materials grows, overcoming these challenges and obtaining a
37 more comprehensive understanding of thermoset fracture at the molecular scale is imperative.

38 In our previous study, we introduced the Machine Learning based Adaptable Bonding Topology
39 (MLABT) framework, an approach tailored for atomistic simulations of thermosets under large de-
40 formation.²² MLABT circumvents limitations of classical molecular dynamics (MD) simulations
41 by integrating a machine learning (ML) algorithm for detection and execution of bond-breaking
42 events (with near QM accuracy) with any underlying classical force-field. Compared to existing

43 methods combining MD and QM,²¹ MLABT exhibits an approximately two orders of magni-
44 tude improved computational efficiency, coupled with heightened sensitivity to rare bond-breaking
45 events at low strains. This blend of speed and accuracy created by augmenting classical force-
46 fields accurate at low strain with QM-quality bond-breaking detection renders MLABT a robust
47 and chemically general tool for probing strain hardening and material failure dynamics in polymer
48 networks.

49 While the development of MLABT is promising for modeling thermoset fracture, it is not with-
50 out its challenges. First and foremost, generating a sufficient volume of training data using QM
51 calculations is resource-intensive. Moreover, provided the rare nature of bond-breaking events,
52 bond evaluations are primarily confined to a narrow strain-hardening window for efficiency rea-
53 sons. Second, existing MLABT training data derives from configurations possessing intact cross-
54 linked topologies, rather than those emerging *in situ* during fracture. These constraints, revolving
55 around inefficient and insufficient configurational sampling, curtail the full potential of MLABT
56 in offering a computationally efficient and molecularly detailed modeling paradigm for thermoset
57 fracture. Recognizing these limitations, the field of active learning (AL),^{23,24} defined by its ability
58 to iteratively refine and expand training datasets, appears an apt fit for these challenges.^{25,26}

59 In this work we integrate AL into MLABT simulations. This provides two concerted benefits
60 for MLABT models: the ability (i) to systematically navigate the vast configurational space of
61 thermoset fracture and (ii) to employ higher accuracy (i.e. more computationally costly) density
62 functional theory (DFT) calculations that better capture the physics of bond breaking, by virtue of
63 using nearly an order of magnitude less training data than previously. Empowered by this AL-DFT
64 MLABT model, we conduct the first comprehensive exploration of thermoset fracture behaviors
65 at the molecular scale using a DFT-accurate bond-breaking model. Note that although classical
66 material fracture involves crack propagation beyond the molecular scale, we use the more specific
67 term “fracture” instead of “failure”, because breaking of the network into two parts can be clearly
68 observed in the simulations, and it is consistent with pre-existing literature studying similar phe-
69 nomena.^{6,7,9} We scrutinize how the stress-strain behaviors as well as bond breakages are modulated

70 by experimental factors including temperature, strain rate, cooling rate, and the degree of crosslink-
 71 ing. The results from our MLABT analysis reveal that strain rates have a more pronounced effect
 72 on bond breakages than temperature, suggesting that the time-temperature superposition principle
 73 does not hold for thermoset plasticity. Importantly, network topology appears to be more influ-
 74 ential than the stability of the glassy structure in determining fracture behavior. Furthermore, we
 75 demonstrate that thermoset stress-strain behavior exhibits small variance under thermal fluctua-
 76 tions, indicating a certain degree of degeneracy in network fracture. Considering that MLABT
 77 leverages the DFT accuracy for bond breaking in fracture modeling, yet doesn't capture the brittle
 78 failure seen in experiments, we conjecture that embracing larger spatiotemporal scales in modeling
 79 will be essential for better alignment with experiments.

80 Methods

81 MLABT simulation

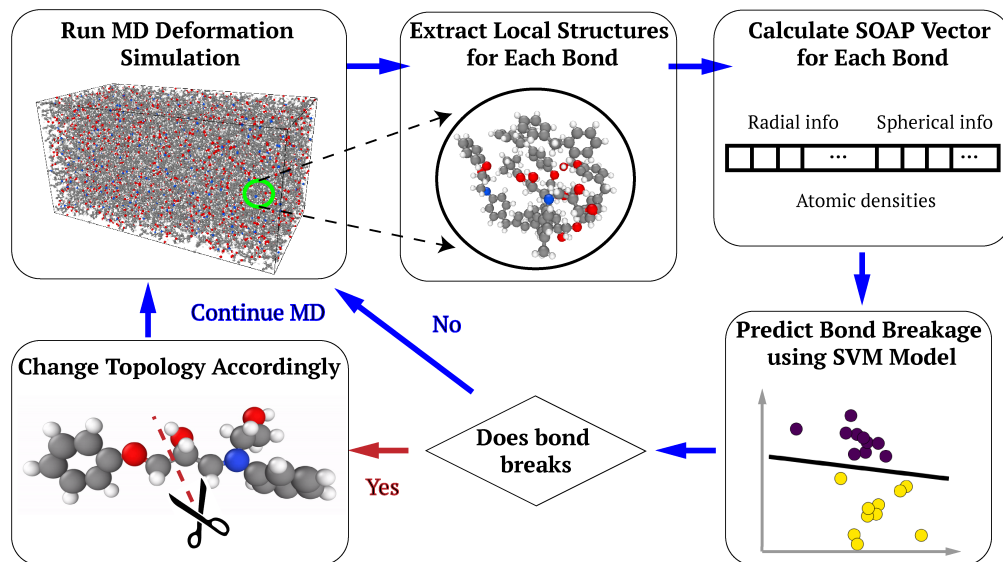


Figure 1: Schematic of the Machine-Learning-based Adaptable Bonding Topology (MLABT) method. MLABT can efficiently predict and perform bond breaking on-the-fly in MD simulations with near quantum-chemical accuracy.²²

82 MLABT is a method incorporated on-the-fly with classical MD (e.g. OPLS, Amber) to accu-

83 rarely describe quantum-chemically accurate bond breaking at dramatically reduced cost, with a
84 focus on the modeling of thermoset deformation and fracture.²² As illustrated in Fig. 1, MLABT
85 scans all potentially breakable bond types in the classical MD simulation and predicts bond rupture
86 based on the local structures. If a bond breaks, the corresponding topology is automatically mod-
87 ified and MD continues until the next bond breaks. We develop MLABT in an archetypal epoxy
88 polymer network, diglycidyl ether of bisphenol A (DGEBA) cured by methylene dianiline (MDA),
89 but the approach is chemically generalizable.

90 We employ similar simulation parameters as described in our previous work.²² Specifically,
91 a cubic box containing 432 DGEBA and 216 MDA molecules (27,432 atoms in total) is utilized
92 with periodic boundary conditions in three dimensions. Bonding topologies of networks are gen-
93 erated dynamically by simulating curing reactions in MD, resulting in degrees of crosslinking
94 ranging from 77% to 98%. Structures are melted at 800 K for 200 ps and then quenched to 300 K
95 with a constant annealing rate ranging from 0.1 K/ps to 100 K/ps. The obtained glassy structures
96 are then used as initial conditions for MLABT deformation simulations. Only uniaxial deforma-
97 tions are considered in this work. During deformations, the simulation box is deformed uniaxially
98 (e.g., along the x axis) every 0.025 ps at a strain rate of 1×10^9 /s and the atomic coordinates are
99 remapped accordingly. The two transverse directions are allowed to relax under $P=1$ atm to avoid
100 the accumulation of artificial stress. We apply the Optimized Potentials for Liquid Simulations All
101 Atoms (OPLS-AA) force-field with the Large-scale Atomic/Molecular Massively Parallel Simu-
102 lator (LAMMPS) in all MD simulations.^{27,28} Simulated glass transition temperature, density, and
103 elastic properties are all in good agreement with experiments and previous simulations.^{11,29-31}

104 Central to MLABT is the ML model tasked with predicting bond breakages by analyzing the
105 bond's instantaneous surroundings. To characterize the local structure, we employ the Smooth
106 Overlap of Atomic Positions (SOAP) descriptor, representing a Gaussian smeared local atomic
107 density based on spherical harmonics and radial basis functions.³²⁻³⁴ We apply the support vector
108 machine (SVM) with the radial basis function kernel as the classifier.³⁵ More details can be found
109 in the reference.²² Considering the additional cost of ML prediction that requires the computation

110 of the SOAP vectors for all the relevant atoms, we perform the scanning of bond breaking every
111 0.001 true strain. In our testing, as long as the evaluation frequency is greater than one check every
112 $\Delta\epsilon = 0.01$, no evident difference is observed in the resultant deformation behavior, as illustrated
113 in Fig. S3 of the Supporting Information. In addition, due to the instability of the structures with
114 broken bonds simulated with OPLS-AA, a timestep of 0.25 fs is utilized in MLABT simulations.
115 Tuning force fields or adding hydrogens to broken bonds could solve this instability issue, but is
116 not performed in the present study. All the simulations conducted in this work are carried out
117 on the Bridges-2 cluster, which is provided by the Advanced Cyberinfrastructure Coordination
118 Ecosystem: Services & Support (ACCESS).³⁶

119 **Iterative MLABT-based active learning**

120 To improve the generalization ability of MLABT across the entire fracture process, the ML model
121 in this work undergoes iterative refinement, enriched progressively by the incorporation of AL. AL
122 is a data-driven methodology primarily aimed at optimizing the process of data labeling and model
123 training.³⁷ Distinct from traditional ML frameworks, where a model is trained on a pre-labeled
124 dataset, AL centers on the model actively selecting the most informative data points from a vast
125 unlabeled pool of data.^{38,39} Here, we harness the power of AL to elucidate the fracture behaviors
126 of thermosets, minimizing costs of QM computations while maximizing predictive generalization
127 ability at diverse deformation conditions.

128 The overall AL workflow is illustrated in Fig. 2. We start sampling highly strained configura-
129 tions in MD simulations and extracting the local structures that potentially contain broken bonds
130 for QM geometry optimization.²² Data pre-screening requires an artificial threshold based either
131 on bond length or stretching energy, which could limit the applicability of the ML model in early
132 bond breaking prediction. To achieve a high fidelity model, we utilize the more accurate DFT
133 method PBEh-3c that improves upon our previous work using the semi-empirical tight-binding
134 method GFN2-xTB.^{22,40} Due to the increased computational cost of PBEh-3c, our computational
135 budget permitted generating a smaller initial training dataset, containing around 5,000 data points.

136 The initial SVM model is fit using 80% of the data and applied to kickstart the AL campaign.

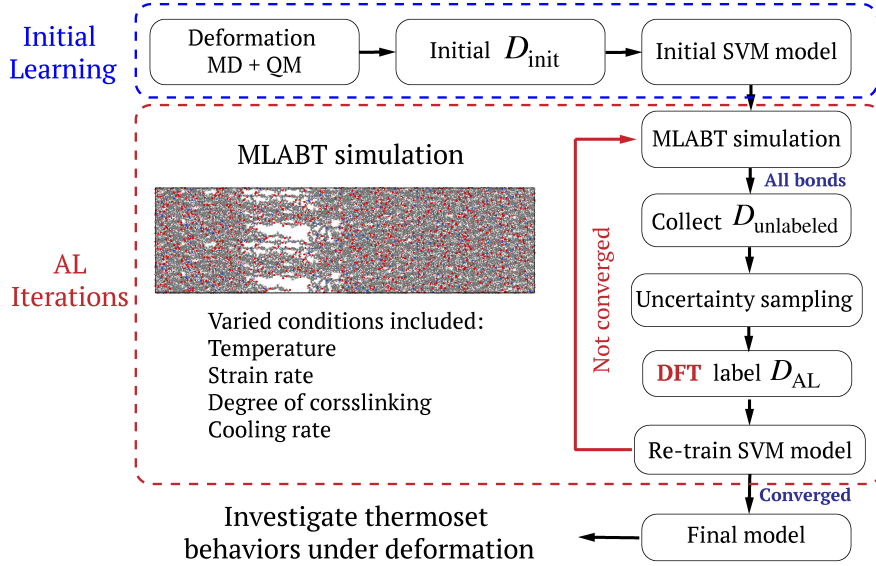


Figure 2: Workflow of the iterative active learning framework for MLABT.

137 To include representative and diverse local structures during deformation into the model train-
 138 ing, we employ an iterative pool-based AL strategy, as illustrated in Fig. 2. In each AL iteration,
 139 we collect all inputs (SOAP vectors) of the potentially breakable bonds (around 4,000 bonds per
 140 frame) in all frames (around 1,250 frames per trajectory) of a MLABT trajectory, which is gener-
 141 ated based on the latest re-trained ML model, as an unlabeled data pool. Note that this step takes
 142 no additional computational cost since SOAP vectors of these bonds were already computed while
 143 performing MLABT simulations. By doing this, the unlabeled data pool in one iteration already
 144 contains comprehensive information of in situ chemical bond local environments within a broad
 145 range of strains throughout the thermoset fracture process. To further improve the model's gener-
 146 alization ability, we introduce some variations in conditions of MLABT simulations during the AL
 147 iterations. In the second iteration, we include simulations at various temperatures from 100 K to
 148 400 K. In the third iteration, we include simulations starting from initial structures with different
 149 bonding topologies. In the fourth iteration, we include simulations with different strain rates and
 150 with initial structures in different degrees of crosslinking (78% to 98%). Over all iterations, around
 151 85 million unlabeled data instances are collected cumulatively for AL querying.

152 **Active learning query strategy**

153 To select the most informative data instances (local configurations) from the large pool of unlabeled
154 data for DFT labeling, we use uncertainty sampling, along with the SVM classifier. In the context
155 of SVM, uncertainty sampling can be intuitively understood by examining the decision function
156 for each prediction.^{41,42} For a data point, the absolute value of the decision function $|f(x)| =$
157 $|\sum_i^N \alpha_i \gamma_i \kappa(x_i, x) + b|$ represents its distance to the decision boundary, where $\kappa(x_i, x) = \langle \phi(x_i) \phi(x) \rangle$
158 is a kernel function and $\alpha_i \gamma_i \phi(x_i)$ forms a weight vector. The smaller this absolute value, the closer
159 the data point is to the decision boundary, which indicates a higher level of uncertainty. Thus,
160 querying data points with the smallest absolute decision functions maximizes the information gain,
161 refining our model with each iteration.

162 However, an inherent challenge emerges when adopting this approach: as our model and data
163 evolve across iterations, the absolute values of the decision function can shift, rendering them non-
164 comparable across different AL cycles. This poses a problem when trying to maintain a consistent
165 measure of uncertainty across multiple iterations. To circumvent this challenge, we employ Platt
166 scaling—a method wherein a logistic regression model is trained using the decision function’s
167 outputs.⁴³ Through this process, the SVM’s raw decision values are transformed into calibrated
168 probabilities, providing a consistent measure of uncertainty irrespective of the active learning it-
169 eration. Within our binary classification context $P(1|x) = 1 - P(-1|x)$, the uncertainty associated
170 with each instance x (SOAP vectors) is defined as

$$u(x) = 1 - \max(P(1|x), P(-1|x)) = 0.5 - |P(1|x) - 0.5| \quad (1)$$

171 Under this formulation, data points with probabilities closer to 0.5 are deemed to have maximum
172 uncertainty, as they lie in regions where the model is most uncertain about its classifications.

173 Using the outlined query strategy, bonds with maximum uncertainty are identified within each
174 snapshot of the MLABT simulation. To regulate the number of bonds selected in each AL iter-
175 ation, we apply an uncertainty threshold of 0.05. For every selected bond, its local environment

¹⁷⁶ is extracted from the large MD configuration. This isolated environment is then subjected to full
¹⁷⁷ optimization via DFT calculations, as in the initial dataset generation.⁴⁴ Each batch of labeled data
¹⁷⁸ from the AL is partitioned into a training set (comprising 80% of the data) and a testing set (ac-
¹⁷⁹ counting for the remaining 20%). Subsequently, the SVM model is retrained, incorporating both
¹⁸⁰ the initial dataset and the cumulative new AL training data. Test data are composed of both the
¹⁸¹ initial data and the cumulative AL test data, as well as unseen data from a new MLABT trajectory
¹⁸² (with maximum uncertainty in every snapshot) based on the final model. Detailed results on the
¹⁸³ model convergence are presented in the subsequent section.

184 **Results**

185 **Active learning performance**

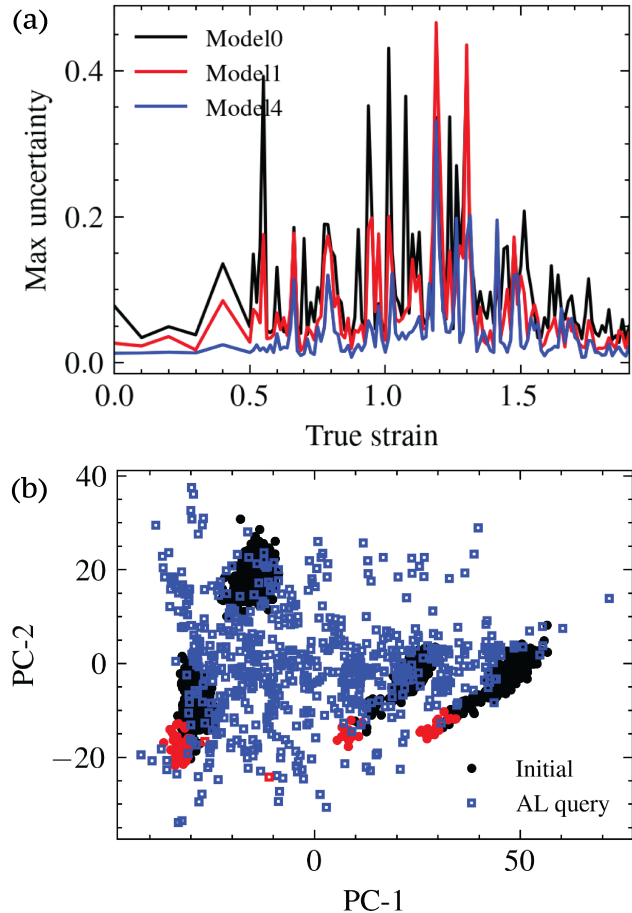


Figure 3: (a) Max uncertainty of bond breaking prediction in MLABT simulations after AL iterations. Uncertainty of bond breaking prediction is computed based on Equation 1, as detailed in the Methods section. ‘Model 0’ denotes the model trained by the initial data, ‘Model 1’ and ‘Model 4’ denotes the updated models after the first and fourth AL iteration, respectively. (b) Initial data and AL data visualized by principle component analysis of the SOAP vectors. The red points represent bonds that are found broken in DFT calculations. The evident difference in data distributions demonstrates that AL explores diverse regions in feature space that are distinct from the initial sampling.

186 The AL framework in this work is based on the query strategy of uncertainty sampling, as detailed
187 in the Methods section. Since bond breaking events are rare even in material fracture, the majority
188 of bond breaking uncertainties are simply zero, even for the initial ML model with a small dataset,
189 as shown in Fig. S1 of the Supporting Information. However, the maximum uncertainty during the

190 deformation could be high if the bond instance lies closer to the poorly trained decision boundary.
191 As shown in Fig. 3A, the initial model shows high peaks in uncertainty around strains of 0.5-
192 0.6, where the bonds start to break, and around strain of 0.9-1.3, where the bonds break rapidly
193 and the resulting stress reaches a maximum. The strain region in between has relatively lower
194 uncertainty, because it is where the initial data are generated. The uncertainty for larger strains
195 (>1.3) decreases, due to weaker interaction between strained bonds in the system that is poorly
196 crosslinked. Nevertheless, the bonds with maximum uncertainty above a threshold of 0.05 in each
197 snapshot are selected, and their local configurations are optimized with DFT to determine bond
198 breaking.

199 Next, we compare the local environments of the AL selected bonds with the bonds in the initial
200 dataset, which are selected by bond stretching energy from configurations in a narrow range of
201 strain, in the reduced dimensions by principle component analysis (PCA). The linear transforma-
202 tion (coefficients) is constructed based on the SOAP vectors of the bonds in the initial dataset. As
203 shown in Fig. 3B, the local environments in the initial dataset form four separated clusters. The
204 right two clusters are associated with the ‘CT-CA’ bonds (connecting the sp³ carbon and the aro-
205 matic carbon) located on both DGEBA and MDA, and the left two clusters are associated with the
206 ‘CT-CT’ bonds on DGEBA. Note that only those ‘CT-CT’ bonds on the DGEBA backbone (the
207 bottom left cluster) are breakable in deformation, while those on DGEBA side chains (the top left
208 cluster) are not. We could remove those from training data, but in this work, they are kept to en-
209 hance generalizability. On the other hand, the local environments selected by AL are scattered over
210 the principal component space and distributed densely in regions between the clusters. This result
211 demonstrates the ability of AL to explore the diverse feature space that is unseen in the initial data.
212 As such, including these AL environments in the model training can improve the generalization
213 ability of MLABT for simulating thermoset deformations under diverse conditions.

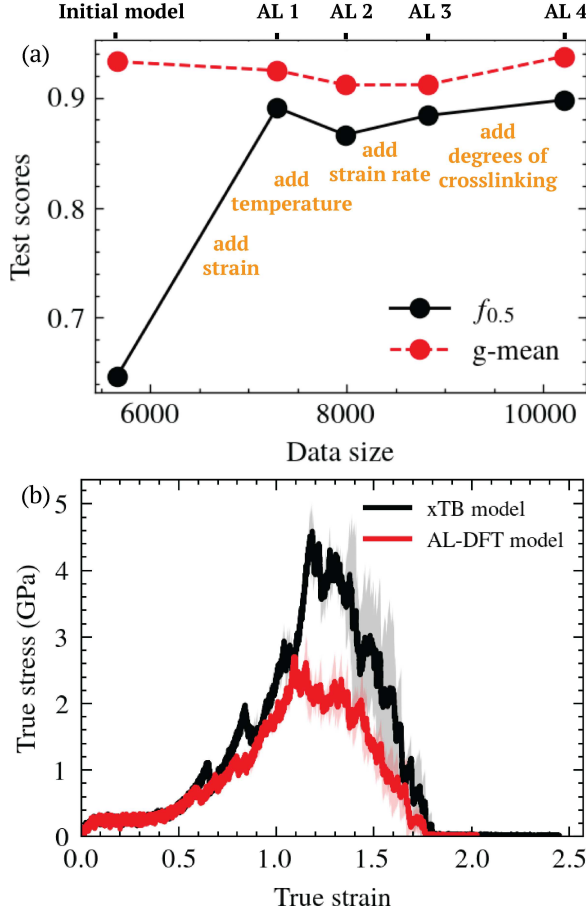


Figure 4: (a) $f_{0.5}$ and geometric mean of the ML model as trained after each AL iteration. (b) Comparison of stress-strain curves simulated by AL-DFT MLABT model and with the xTB MLABT model at 300 K with a strain rate of 10^9 /s. The xTB MLABT model overestimates the ultimate stress, compared to the AL-DFT model and previous simulations.⁴⁵ The shadow regions represent the standard deviations induced by randomness in initial velocity generation over three independent trajectories (same for subsequent figures).

Figure 4A shows the performance of the ML model on the test set after each AL iteration. The selection of the scoring metrics considering the imbalanced classification was discussed in previous work.^{22,46} It can be seen that the initial model exhibits an excellent geometry mean, whereas $f_{0.5}$ is relatively low, indicating a higher rate of false positives on regions outside of the initial training region. Once the model is updated with the AL selected data from the entire strain range using varied deformation and temperatures, $f_{0.5}$ improves immediately while geometric mean remains almost unchanged. With more AL iterations including deformations using various strain rates and configurations with various degrees of crosslinking, the performance of the model remains

almost unchanged, whereas the maximum uncertainty decreases evidently (Fig. 3). After the fourth AL iteration, the maximum uncertainty is almost zero before the first bond breaking, and it remains above 0.15 only in a narrow strain range around 1.2. This performance is reflected in the distribution of prediction uncertainty, as shown in Fig. S1B and S1C of the Supporting Information. In addition, the number of bonds in the same deformation trajectory with uncertainty above 0.05 decreases with more AL iterations, but the rate of decrease slows after the second iteration, as shown in Fig. S2A of the Supporting Information. These features all suggest that the model in the AL framework is converging. To confirm the convergence, we apply the models after each iteration in MLABT simulations with identical initial conditions (positions, velocities). The results of the models after the second iterations are very similar, especially at $\epsilon < 1.5$, as shown in the Fig. S2B of Supporting Information. As such, we end the AL campaign and employ the model after the fourth iteration as the final model (denoted as ‘AL-DFT’) in this work for further investigation.

MLABT simulations with the new AL-DFT MLABT model provide more accurate results on thermoset fracture than with the previously reported ‘xTB’ MLABT model. As shown in the stress-strain curves (SSC) in Fig. 4B, although the two models produce similar strains for the fracture initiation (the first bond breaking), the ultimate stress, and the material failure, the ultimate stress of AL-DFT MLABT is roughly one half of that of xTB MLABT, showing improved agreement with previous simulations (1-3 GPa).⁴⁵ This reduced ultimate stress is induced by an increase of broken bonds and already appears in the initial model, suggesting that the GFN2-xTB method compared to DFT underestimates the probability of bond breaking. In addition, we find that simple models only using bond length as the breakage criterion, as reported in earlier simulations,^{21,47} could delay early bond breaking events and fail to generalize across various thermodynamic or morphological conditions, as detailed in the Supporting Information (Fig. S4). Furthermore, the shadow regions in Fig. 4B shows the standard deviation caused by randomness in velocity initialization, i.e., random seeds in generating initial atom velocities from the Maxwell–Boltzmann distribution. Although the specific broken bonds and locations are different, the overall variance in the SSC during strain

249 hardening is small. This suggests that there is some degeneracy in fracture initiation sites during
250 thermoset deformation that result from velocity initialization, but they weakly affect the overall
251 mechanical properties. The variation of ultimate stress and failure is stronger, probably due to the
252 accumulated differences in bond breaking resulting in evident differences in the broken topology.
253 We note that to our knowledge this study represents the first QM-informed atomistic study to report
254 error bars in stress-strain curves of thermoset fracture, as for traditional approaches such error bars
255 would be too computationally costly to compute.

256 **Bond breaking during deformation**

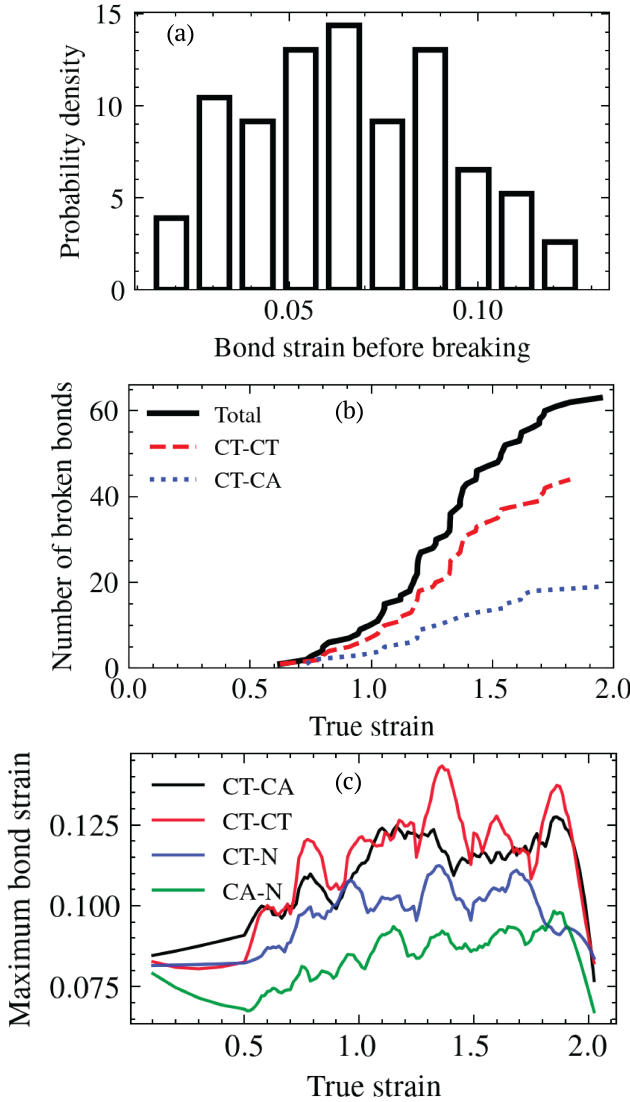


Figure 5: (a) Bond strain distribution immediately before bond breakage during MLABT simulations in the highly crosslinked system (98%) at 300 K with a strain rate of 10^9 /s. (b) The numbers of broken bonds in the two dominant broken bond types as a function of strain. (c) The maximum bond strains for various bond types in the system as a function of strain. The bond strain is defined as $(l - l_0)/l_0$, where l is the instantaneous bond length and l_0 is the equilibrium bond length.

257 The more accurate AL-DFT MLABT model enables investigation of the bond breaking chemistry
 258 during thermoset fracture. Figure 5A shows the distribution of bond strain, defined as $(l - l_0)/l_0$,
 259 where l is the instantaneous bond length and l_0 is the equilibrium bond length, immediately before
 260 bond breaking during MLABT simulations in the highly crosslinked system (98%) at 300 K with

261 a strain rate of 10^9 /s. Similar results are observed at other conditions. It is surprising that the
262 bond breakages occur at much smaller bond strains than previously expected.⁴⁸ The maximum
263 value around 0.12 is even smaller than the threshold value used in Barr's method for pre-screening
264 local configurations that potentially contain broken bonds,²¹ suggesting that the methods based on
265 artificial criteria and QM calculations can delay bond breaking during deformation.

266 The actual types of broken bonds in MLABT simulations of thermoset fracture are found to
267 align with those revealed in QM calculations. Note that although we observed two types of broken
268 bonds in strained DGEBA+MDA by QM calculations (both DFT and xTB), it does not guarantee
269 these two types are actually broken during thermoset fracture because the local environments with
270 evolving topology could become very different. As shown in Fig. 5B, the numbers of broken bonds
271 decomposed into the two types show a consistent ratio throughout the entire fracture process. This
272 ratio, i.e., approximately 2:1 for 'CT-CT' and 'CT-CA', is in agreement with the observations in the
273 DFT calculations. This suggests that the bond breaking mechanism in epoxy thermosets remains
274 consistent during fracture, independent of global strain. Furthermore, because our ML model is
275 designed for only predicting these two types, we need to evaluate the possibility of bond breaking
276 in other bond types during fracture. Figure 5C illustrates the maximum bond strain for four types
277 of potentially broken bonds in the entire MLABT simulation. The 'CT-CT' and 'CT-CA' bonds
278 indeed exhibit the highest maximum bond strain, with 'CT-CT' frequently being slightly higher
279 than 'CT-CA'. This is consistent with the fact that only these two types were broken and that 'CT-
280 CT' bonds have a higher probability of rupture. The maximum bond strain of 'CT-N' or 'CA-N'
281 are evidently lower and cannot exceed those of the two broken types in the entire fracture range,
282 confirming that they cannot break and negligibly contribute to the ML bond breaking model.

283 **Fracture behaviors by MLABT**

284 Utilizing AL-DFT MLABT simulations, we can efficiently probe the fracture behaviors of poly-
285 mer networks at the atomic scale, combining the molecular precision and computational efficiency
286 of classical MD with bond-breaking fidelity approaching that of DFT. It is imperative to recognize,

287 however, that both the lengthscale and timescale exert significant influence on the network topol-
 288 ogy's formation and its dynamical response. We focus on extracting physical insights, specifically
 289 examining how the bond breaking events and fracture behaviors of polymer networks are modu-
 290 lated by factors such as temperature, strain rates, cooling rates, and the degree of crosslinking.

291 **Temperature effect**

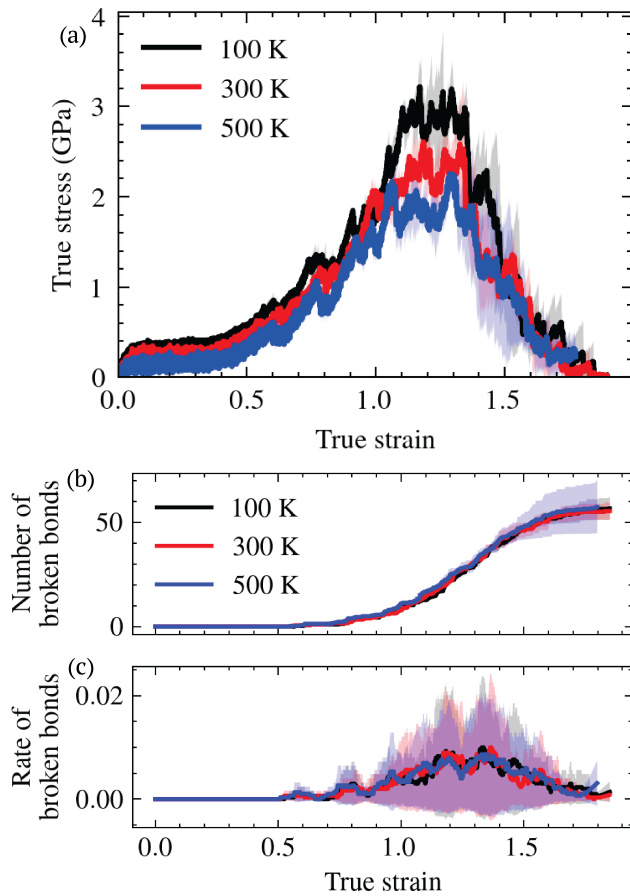


Figure 6: (a) Stress-strain curves of the same initial structure (98% crosslinked) simulated by AL-DFT MLABT at three temperatures with the same strain rate of $10^9/\text{s}$. (b)-(c) Corresponding accumulated number and rate of the bond breaking events during deformation. The unitless rate in (c) is simply the derivative of the accumulated number in (b), with smoothing and normalization for better visualization. The shadow regions represent the standard deviations induced by randomness in initial velocity generation over three independent trajectories, and the curves represent the averaged results. The same settings are applied in subsequent figures.

292 First, we assessed the impact of temperature, held constant during deformation, on the fracture
 293 behavior of thermosets. Figure 6 displays (a) the SSC, (b) the count of broken bonds, and (c) the

294 rate of bond breakage (as deduced from the slope in (b)) at three distinct temperatures, 100 K, 300
295 K, and 500 K, in MLABT simulations of a 98% crosslinked system subjected to a strain rate of
296 $10^9/\text{s}$. These temperatures are all below the glass transition temperature ($T_g \sim 541 \text{ K}$). In general,
297 bond breaking events appear temperature-insensitive, with temperature only influencing theulti-
298 mate stress as a consequence of the temperature effect before yielding. Specifically, a decrease in
299 temperature enhances the elastic modulus and the corresponding yield stress, in agreement with
300 previous experiments and simulations.⁴⁹ However, the frequency of bond breakage events remain
301 consistent in the plastic regime, and consequently, the characteristic strains for fracture initiation,
302 peak stress, and ultimate failure also exhibit temperature independence. Only the stresses during
303 strain softening and hardening vary as a result of the effect on the elastic regime, which was also
304 observed in previous MD simulations without considering bond breaking.⁵⁰ These findings suggest
305 that bond rupture in amorphous polymer networks may not be characterized as a simple activation
306 reaction. The potential reason may be related to heterogeneous local stresses that arise depending
307 on the global strain and the network topology.^{51,52} Additional temperature-dependent behaviors in
308 experiments, such as increased brittleness at lower temperatures,⁵³ could be attributed to factors
309 like crystallinity, entanglements, or effects occurring over extended spatiotemporal scales.

310 Moreover, we find that the resultant stress is generally correlated with the bond breakage rate,
311 a trend consistently observed across all conditions evaluated in this study. As the count of bonds
312 on the edge of breaking surges during strain hardening, the cumulative stress also rises until the
313 bond breakage rate peaks, resulting in the ultimate stress. Following this, as the bond breaking rate
314 diminishes, so does the stress, until failure ensues. In addition, the thermal fluctuations mediated
315 by random initial velocity generation show a relatively small impact on the number of broken bonds
316 and the stress response during network deformation, though the bond breaking rate can fluctuate
317 more strongly (in Fig. 6c) due to discreteness and randomness in individual bond breakages. The
318 total count of bonds required to rupture the thermoset is approximately 55, around 0.2% of the
319 total bonds or 1.5% of the potentially breakable bond types in the system, which is notably smaller
320 than the number of reactions needed for network gelation.

321 **Strain rate effect**

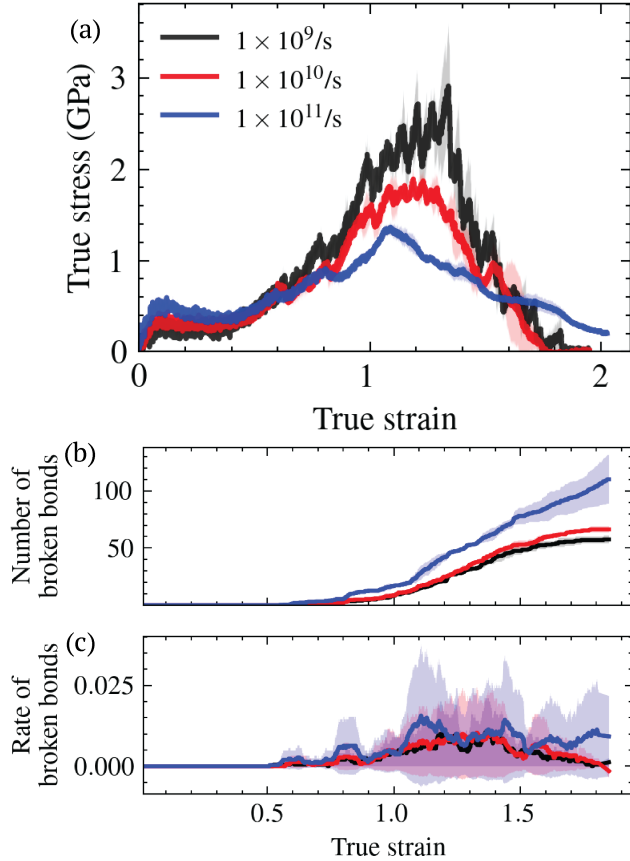


Figure 7: (a) Stress-strain curves of the same initial structure (98% crosslinked) simulated by MLABT with three strain rates at 300 K. (b)-(c) Corresponding number (b) and rate (c) of the bond breaking events during deformation.

322 Next, we investigate the effect of strain rate on the thermoset fracture behavior. As shown in Fig. 7,
 323 distinct from temperature, strain rate not only strongly affects the elastic behavior but also plastic
 324 and fracture behaviors. In the elastic regime, a larger strain rate results in higher elastic modulus
 325 and yield stress (Fig 7A), in agreement with previous experiments and simulations.^{47,48,54–56} Thus,
 326 a more noticeable strain softening regime is observed at larger strain rates. More interestingly, the
 327 bond breaking occurs more rapidly at higher strain rates, although the characteristic strains for
 328 fracture initiation (first bond breaking) and ultimate stress are almost independent of strain rate,
 329 as shown in Fig. 7B and C. Consequently, more bonds are broken in deformation with a large
 330 strain rate and the resultant ultimate stress is evidently reduced. The reason for this result is that

331 at large strain rates with little stress release, bond breakages do not occur in the most productive
332 way, i.e., breaking apart the network using as few cuts as possible. Hence, the system could
333 remain connected even though a large number of bonds have broken, and as a result, the system
334 exhibits reduced ultimate stress and behaves more ductile at large strain rates, as shown in Fig. 7A.
335 Note that this effect might converge at low strain rates, as the stress is fully relaxed once a bond
336 breaks when the associated timescale is closer to or even longer than the stress field propagation
337 time, which is supported by the smaller difference in the effect when changing the strain rate from
338 $10^{10}/\text{s}$ to $10^9/\text{s}$. Nevertheless, the MLABT results suggest a distinct disparity between effects of
339 strain rate and temperature within the plastic regime. A further demonstration on the breakdown
340 of their superposition is provided in the Supporting Information.

341 **Cooling rate effect**

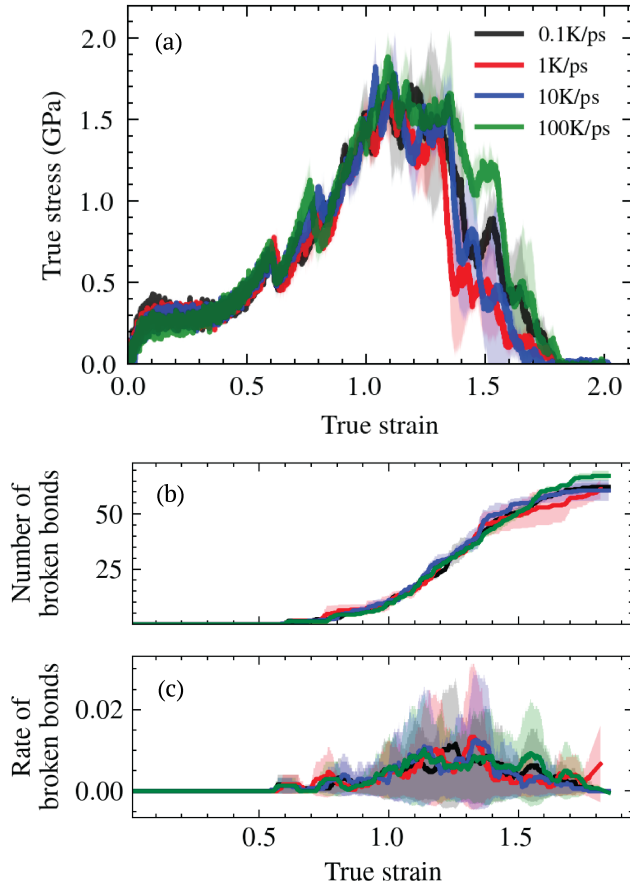


Figure 8: (a) Stress-strain curves of polymer networks with the same topology (98% crosslinked) but generated with different annealing (cooling) rates simulated by MLABT at 300 K and with a strain rate of $10^{10}/\text{s}$. (b)-(c) Corresponding numbers and rates of the bond breaking events during deformation.

342 Furthermore, we study the effect of cooling rate in the melt-quenching process for synthesizing
 343 glassy thermosets on its bond breaking and fracture behavior by MLABT simulations. As glass
 344 is a non-equilibrium state below the glass transition, the cooling rate and the associated timescale
 345 for relaxation controls the temperature at which the supercooled liquid loses ergodicity and the
 346 amorphous structure becomes “frozen”.⁵⁷ Specifically, a smaller cooling rate results in a lower
 347 glass transition temperature, and thereby, a thermodynamically more stable glass state, i.e., a state
 348 located lower in the potential energy landscape. These more stable glasses show distinct atomic
 349 structures and materials properties compared to glasses with higher cooling rates, such as higher

350 density and higher mechanical strength.^{58,59} Such a cooling rate effect is observed in the elastic
351 regime of thermosets, as shown in Fig. 8A, as the elastic modulus and yield stress increase with
352 reduced cooling rates (details summarized in Table S1 of the Supporting Information). Note that
353 in the simulations, the initial structures have identical bonding topology but only are generated by
354 different cooling rates in melt-quenching simulations initial configurations from 800 K to 300 K
355 prior to deformation. Interestingly, the cooling rate effect does not survive in the plastic behaviors.
356 As strain increases in the strain softening and the initial part of the strain hardening (till strain~0.6),
357 the difference of stress induced in the elastic regime gradually disappears, suggesting that the
358 effect of the initial glassy structures diminishes. Consequently, the following bond breaking effects
359 and the fracture behavior are independent of the cooling rate, as shown in Fig. 8A-C. These
360 observations can be understood by considering that the cooling rate in general determines the
361 stability of initial glassy structures and therefore controls the elastic behavior (without structural
362 change), however, as strain increases, the strain-induced structural modulation becomes dominant
363 through the covalent bonded network, and the difference in the amorphous strained structures
364 becomes negligible. We should also note that this limited cooling rate effect is an outcome of
365 strong topological constraints of thermosets and the short length of strands used in the simulations.

366 **Effect of crosslinking degree**

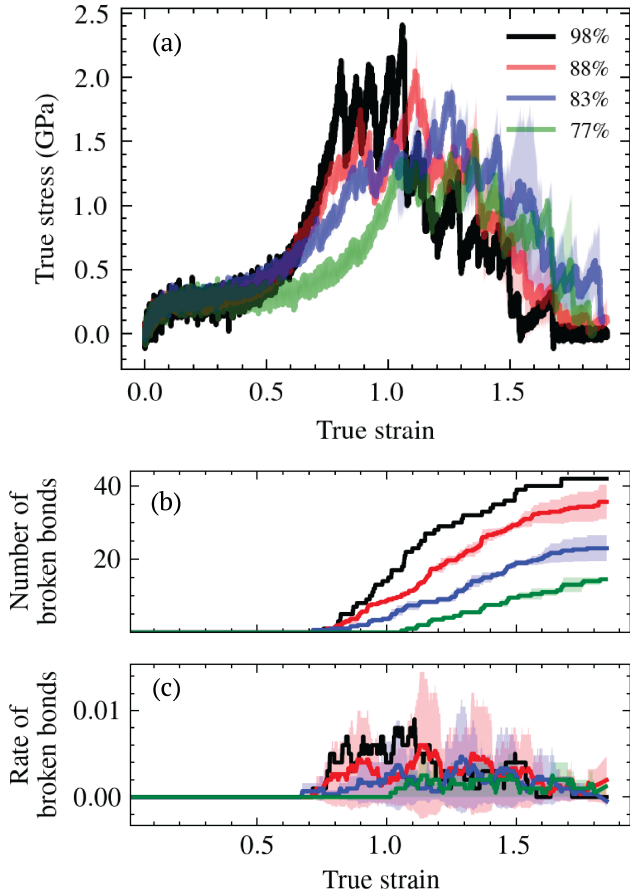


Figure 9: (a) Stress-strain curves simulated by MLABT for structures with different degrees of crosslinking at 300 K and with a strain rate of $10^9/\text{s}$. (b)-(c) Corresponding numbers and rates of the bond breaking events during deformation.

367 Finally, we study how the degree of crosslinking affects bond breakage and fracture behavior of
 368 thermosets by MLABT simulations. In this work, the crosslinks are formed dynamically in MD
 369 simulations of curing reactions, and thus the degree of crosslinking is controlled by how long
 370 the curing process runs. As shown in Fig. 9, we prepare four structures with various degrees of
 371 crosslinking from 77% to 98% (all gels) and simulate their deformation responses with MLABT
 372 at 300 K with a strain rate of $10^9/\text{s}$. Note that in this work, we do not provide statistically averaged
 373 results over various bonding topologies due to computational cost, however, the structures eval-
 374 uated herein with the four degrees of crosslinking are generated from the same curing reaction in an
 375 effort to emphasize the influence of crosslinking degree.

376 In the system with a higher degree of crosslinking, while the elastic behaviors are subtly
377 changed (due to smaller variations of crosslinking density⁶⁰), the SSC in strain hardening in-
378 creases more rapidly, and reaches the ultimate stress at a smaller strain value, as shown in Fig.
379 9A. As the degree of crosslinking decreases, the ultimate stress shifts to a larger strain and the
380 peak value decreases. Specifically, when the crosslinking degree decreases from 98% to 77%, the
381 ultimate stress decreases by roughly 1/3 and the corresponding true strain increases by 1/3. This
382 is generally consistent with results of previous simulations using ReaxFF.⁴⁵ This behavior of SSC
383 can be understood from bond breakages in Fig. 9B and C. As expected, fewer bonds are broken in
384 systems with lower crosslinking degrees, consistent with the lower ultimate stress values. More-
385 over, the dominant bond breaking events, indicated by the maximum rate of bond breaking, occur
386 at larger strains, accounting for the shift of ultimate strain. Depending on specific modification of
387 bonding topology, the strain of fracture initiation might shift such that it is delayed to a larger strain
388 at a crosslinking degree of 77%. We also note that although the effect of crosslinking degree is
389 revealed here, the relationship between network fracture and network topology is intriguing yet
390 more complex (the variance induced by topology at same degrees of crosslinking is illustrated in
391 Fig. S7 of the Supporting Information), which warrants further investigation.

392 Discussion

393 The AL-DFT MLABT framework stands out as a promising approach for accurately modeling
394 thermoset fracture, as bond breaking during fracture is performed at nearly quantum chemical
395 accuracy while computational cost is kept similar to that of classical MD. Specifically, the AL
396 modification of MLABT presents two distinct advantages: i) Integration of AL enables incorpo-
397 ration of diverse training data across thermodynamic and configurational conditions, improving the
398 transferability of models to new conditions. ii) By actively pinpointing the most informative data
399 for training, the AL framework is roughly an order of magnitude more efficient in the generation
400 of training data than our previous MLABT model. This heightened efficiency permits utilization

401 of more accurate (and computationally costly) QM methods, such as DFT.

402 Importantly, these two advantages of the AL-DFT MLABT framework manifest in the po-
403 tential generalizability of the methodology across chemical space, an area where other reactive
404 models (e.g. ReaxFF) can struggle. As MLABT leverages widely-accepted classical force-fields,
405 such as OPLS and Amber, as its baseline simulation method, the high performance of common
406 quantities such as density and low strain mechanical response is ensured across a broad chemical
407 space. By adding on a QM-quality bond breaking prediction, mediated by ML, to these classical
408 simulations, the MLABT approach is inherently adaptable to new chemistries for which accurate
409 classical force-fields exist. Moreover, the ML component responsible for bond breaking is also
410 inherently adaptable as it leverages structural representations (SOAP vectors) and is informed by
411 QM calculations, making it agnostic to specific chemistries. This flexibility allows for the effi-
412 cient adaptation of the MLABT framework to new chemistries, a process further streamlined by
413 the AL approach introduced in this study. In contrast, empirical methods like ReaxFF demand
414 a cumbersome and iterative parameterization process.⁶¹ Transferability of the parameter sets in
415 ReaxFF is a well-known (and expected) deficiency compared to classical FF as the prediction task
416 required is more challenging.⁶² In our testing as detailed in the supporting information, MLABT
417 and ReaxFF show generally consistent results in modeling network deformation, particularly on
418 the overall bond breakages. However, without constant computation of charge and bond topology
419 as in ReaxFF, MLABT is computationally more efficient by at least one order of magnitude. Pro-
420 vided these advantages, MLABT may be a suitable and easily implementable alternative to ReaxFF
421 for unparameterized chemistries, especially when a trusted classical FF is already known.

422 As mentioned in the Methods section, a minor limitation of the current MLABT implementa-
423 tion is the necessity for a small timestep (0.25 fs as opposed to 1 fs commonly used in standard MD
424 simulations). This issue is primarily due to the instability introduced by broken bonds when using
425 classical force fields. However, this drawback can be fixed in future developments of MLABT, ei-
426 ther through optimizing the force fields or by appending hydrogens to atoms involved in the bond
427 rupture. Importantly, the MLABT simulations conducted in this study did not employ these modi-

428 fication, ensuring that our reported outcomes remain free from any influence of mechanoradicals
429 that could otherwise alter network dynamics and subsequent bond breakages. The role of these
430 mechanoradicals in subsequent bond breaking processes is a challenging topic reserved for future
431 works.

432 The computational efficiency of MLABT relative to other QM-informed bond-breaking ap-
433 proaches also enables a number of crucial insights into the nature of fracture in epoxy thermosets.
434 Specifically, we are able to simulate multiple replicas of our networks both in phase space and
435 topology with DFT accuracy at minimal computational cost. From this added computational sam-
436 pling, we observe that thermal fluctuations in the fracture process (as mediated by differing initial
437 seeds in the velocity distribution) have a small impact on the resulting fracture process until the
438 point of material failure. Although the exact bond breaking sites can differ due to randomness in
439 the initial velocity distribution, the variations in the SSC and bond breaking are small during strain
440 hardening. After the ultimate stress, these variations become larger due to accumulated topological
441 differences.

442 Importantly, the MLABT results demonstrate that the polymer network topology plays a more
443 important role in controlling fracture behavior than fine details of the polymer's glassy structure.
444 Specifically, although the elastic mechanical properties depend on the cooling rate in the melt-
445 quenching of thermosets, the plastic properties and bond breakages are independent of it (Fig. 8),
446 suggesting that the influence of glassy structure blurs due to strain-induced rearrangement beyond
447 the elastic regime. On the other hand, the degree of crosslinking (Fig. 9) and the topology varia-
448 tion at the same degree (Fig. S7) primarily determine the fracture behavior, such as the ultimate
449 strain/stress and the fraction of broken bonds. This again confirms the importance of topological
450 perspective for understanding the fracture mechanisms of polymer networks.^{7,9,63}

451 Lastly, our results show that time and temperature, the superposition of which is often posited
452 to understand the viscoelastic behaviors of polymers, play different roles in the network fracture.
453 Specifically, temperature does not affect bond breakages but slightly changes the resultant stress
454 due to the local relaxation of glassy structures. However, the strain rate can strongly determine the

455 strain-stress behavior by influencing the rate of bond breakages. At large strain rates, the strain-
456 induced structural evolution can propagate faster than the release of stress via network topology
457 immediately after bond scission. As a consequence, additional “unnecessary” bonds break, result-
458 ing in a more fragile network with lower ultimate stress. Note that although this physical scenario
459 seems reasonable from the atomistic perspective (also supported by the ReaxFF results in Fig. S6
460 of the Supporting Information), it cannot explain the general trend observed in experiments that a
461 decrease in temperature or an increase in strain rate leads to more brittle fracture behaviors. The
462 reason is that in experiments where deformation is much slower compared with stress release, the
463 bond breakages can occur in the most efficient way through networks and the difference in fraction
464 of broken bonds is tiny when varying deformation rates. This is consistent with the simulation
465 results in Fig. 7b where the differences become smaller when further decreasing the strain rate,
466 suggesting a possible convergence at strain rates close to those used in experiments. As such, the
467 ultimate stress on experimental timescales will be dominated by stress relaxation due to structural
468 reorganization. This is confirmed by our simulation results that show the stress after structural op-
469 timization at each deformation step is much lower than that without optimization, as shown in Fig.
470 S9 in the Supporting Information. In this context, the strain rate effect reported in the MLABT
471 simulations is mainly due to bond breaking events rather than long-term structural relaxation.

472 More importantly, the discrepancy with experiments is reflected in the long-recognized anomaly
473 of ductile fracture in the molecular modeling of thermosets,^{64,65} a phenomenon whose root cause
474 is still under debate.⁶⁶ Given that the MLABT method offers QM-level accuracy in bond breaking,
475 yet still demonstrates ductile fracture, and considering the revealed atomistic strain-rate effect is
476 unlikely to contribute to a brittle fracture (when extrapolated at experimental strain rates), mod-
477 eling at larger length scales is imperative to bridge the gap between experiments and simulations.
478 One reason is that for typical simulation length scales, the crosslinking density (~ 0.1 mole/cm³)
479 significantly exceeds the experimental values (0.001-0.01 mole/cm³).^{67,68} This discrepancy hin-
480 ders the formation of polymer chain entanglements in current molecular dynamics simulations of
481 thermosets. Another hypothesis is related to larger-scale structures, such as air pockets or pores.

482 Air pockets or pores could potentially expedite the fracture towards the elastic regime and exhibit
483 a distinct temperature dependence through micro-structural reorganization.^{69–71} One piece of sup-
484 porting evidence is that in experiments of thermoset films where length-scales are limited below
485 micrometers, the elongation can exceed 100% before failure,⁷² in better alignment with the be-
486 haviors in the simulations. These factors also contribute to the ultimate strength at fracture of the
487 material in the present simulations being greater than those in experiments. More detailed dis-
488 cussions are provided in the Supporting Information. Nevertheless, we believe that incorporating
489 larger length-scale structures in modeling is a promising direction for resolving these discrepan-
490 cies, and MLABT, owing to its efficient and accurate treatment of bond breaking, is well-suited for
491 extending to larger length-scales in diverse environments, including composites and interfaces.

492 Conclusion

493 We have combined AL with MLABT to create a framework for the atomistic modeling of ther-
494 moset fracture with DFT-accuracy and classical FF cost. This integration offers heightened pre-
495 dictive accuracy across thermodynamic and configurational space while simultaneously improving
496 efficiency during model training. Moreover, the adaptability of MLABT with AL enables re-
497 searchers to explore polymer fracture across diverse chemistries, provided a suitable classical FF,
498 avoiding the pitfalls of cumbersome parameterization in other reactive methods. We have applied
499 the MLABT framework to understand the molecular determinants of fracture in polymer networks,
500 finding that the network topology largely dictates fracture behaviors, while the intrinsic stability
501 of the glassy structures has little influence. Interestingly, strain rate, rather than temperature, pre-
502 dominantly impacts network fracture at atomic scale, deviating from conventional paradigms in
503 elasticity. Looking ahead, MLABT-based models of thermoset fracture form a potentially useful
504 basis for the establishment of chemically generalizable bond-breaking models applicable to a di-
505 verse set of polymer chemistries while leveraging the vast array of existing, and high-accuracy,
506 classical force-fields.

507 **Supporting Information**

508 Uncertainty and convergence of the AL MLABT model, effect of MLABT bond scanning fre-
509 quency on failure, comparison of MLABT with a simple model based on bond lengths, comparison
510 of MLABT with ReaxFF, effect of network topology on fracture, time-temperature superposition
511 in polymer network fracture, discussion on discrepancies with experiments.

512 **Acknowledgement**

513 This material is based upon work supported by the National Science Foundation Chemical The-
514 ory, Models, and Computation division under award CHE-2154916. This work used Bridges-2 at
515 the Pittsburgh Supercomputing Center through allocation CHE230055 from the Advanced Cyber-
516 infrastructure Coordination Ecosystem: Services & Support (ACCESS) program, which is sup-
517 ported by National Science Foundation grants #2138259, #2138286, #2138307, #2137603, and
518 #2138296.

519 **References**

520 (1) Jayan, J. S.; Appukuttan, S.; Wilson, R.; Joseph, K.; George, G.; Oksman, K. In *Fiber Rein-
521 forced Composites*; Joseph, K., Oksman, K., George, G., Wilson, R., Appukuttan, S., Eds.;
522 Woodhead Publishing Series in Composites Science and Engineering; Woodhead Publishing,
523 2021; pp 1–24.

524 (2) Auvergne, R.; Caillol, S.; David, G.; Boutevin, B.; Pascault, J.-P. Biobased Thermosetting
525 Epoxy: Present and Future. *Chem. Rev.* **2014**, *114*, 1082–1115.

526 (3) Jin, F.-L.; Li, X.; Park, S.-J. Synthesis and Application of Epoxy Resins: A Review. *Journal
527 of Industrial and Engineering Chemistry* **2015**, *29*, 1–11.

528 (4) Post, W.; Susa, A.; Blaauw, R.; Molenveld, K.; Knoop, R. J. I. A Review on the Potential and

529 Limitations of Recyclable Thermosets for Structural Applications. *Polymer Reviews* **2020**,
530 *60*, 359–388.

531 (5) Gioia, C.; Lo Re, G.; Lawoko, M.; Berglund, L. Tunable Thermosetting Epoxies Based on
532 Fractionated and Well-Characterized Lignins. *J. Am. Chem. Soc.* **2018**, *140*, 4054–4061.

533 (6) Rottler, J. Fracture in Glassy Polymers: A Molecular Modeling Perspective. *J. Phys.: Con-*
534 *dens. Matter* **2009**, *21*, 463101.

535 (7) Barney, C. W.; Ye, Z.; Sacligil, I.; McLeod, K. R.; Zhang, H.; Tew, G. N.; Riggleman, R. A.;
536 Crosby, A. J. Fracture of Model End-Linked Networks. *Proceedings of the National Academy*
537 *of Sciences* **2022**, *119*, e2112389119.

538 (8) Wang, S.; Panyukov, S.; Craig, S. L.; Rubinstein, M. Contribution of Unbroken Strands to
539 the Fracture of Polymer Networks. *Macromolecules* **2023**, *56*, 2309–2318.

540 (9) Stevens, M. J. Interfacial Fracture between Highly Cross-Linked Polymer Networks and a
541 Solid Surface: Effect of Interfacial Bond Density. *Macromolecules* **2001**, *34*, 2710–2718.

542 (10) Sbrescia, S.; Ju, J.; Creton, C.; Engels, T.; Seitz, M. Effect of Temperature, Rate, and Molec-
543 ular Weight on the Failure Behavior of Soft Block Copoly(Ether–Ester) Thermoplastic Elas-
544 tomers. *Soft Matter* **2023**, *19*, 5127–5141.

545 (11) Ortiz, C.; Kim, R.; Rodighiero, E.; Ober, C. K.; Kramer, E. J. Deformation of a Polydomain,
546 Liquid Crystalline Epoxy-Based Thermoset. *Macromolecules* **1998**, *31*, 4074–4088.

547 (12) Glotzer, S. C.; Paul, W. Molecular and Mesoscale Simulation Methods for Polymer Materials.
548 *Annual Review of Materials Research* **2002**, *32*, 401–436.

549 (13) Wu, C.; Xu, W. Atomistic Molecular Modelling of Crosslinked Epoxy Resin. *Polymer* **2006**,
550 *47*, 6004–6009.

551 (14) Zhong, M.; Wang, R.; Kawamoto, K.; Olsen, B. D.; Johnson, J. A. Quantifying the Impact of
552 Molecular Defects on Polymer Network Elasticity. *Science* **2016**, *353*, 1264–1268.

553 (15) Odegard, G. M.; Jensen, B. D.; Gowtham, S.; Wu, J.; He, J.; Zhang, Z. Predicting Mechanical
554 Response of Crosslinked Epoxy Using ReaxFF. *Chemical Physics Letters* **2014**, *591*, 175–
555 178.

556 (16) Li, C.; Strachan, A. Molecular Scale Simulations on Thermoset Polymers: A Review. *Journal*
557 *of Polymer Science Part B: Polymer Physics* **2015**, *53*, 103–122.

558 (17) Hsu, Y.-C.; Yu, C.-H.; Buehler, M. J. Using Deep Learning to Predict Fracture Patterns in
559 Crystalline Solids. *Matter* **2020**, *3*, 197–211.

560 (18) Buehler, M. J. Modeling Atomistic Dynamic Fracture Mechanisms Using a Progressive
561 Transformer Diffusion Model. *Journal of Applied Mechanics* **2022**, *89*.

562 (19) Wang, S.; Hu, Y.; Kouznetsova, T. B.; Sapir, L.; Chen, D.; Herzog-Arbeitman, A.; John-
563 son, J. A.; Rubinstein, M.; Craig, S. L. Facile Mechanochemical Cycloreversion of Polymer
564 Cross-Linkers Enhances Tear Resistance. *Science* **2023**, *380*, 1248–1252.

565 (20) Zhao, X.; Chen, X.; Yuk, H.; Lin, S.; Liu, X.; Parada, G. Soft Materials by Design: Uncon-
566 ventional Polymer Networks Give Extreme Properties. *Chem. Rev.* **2021**, *121*, 4309–4372.

567 (21) Barr, S. A.; Kedziora, G. S.; Ecker, A. M.; Moller, J. C.; Berry, R. J.; Breitzman, T. D. Bond
568 Breaking in Epoxy Systems: A Combined QM/MM Approach. *J. Chem. Phys.* **2016**, *144*,
569 244904.

570 (22) Yu, Z.; Jackson, N. E. Machine Learning Quantum-Chemical Bond Scission in Thermosets
571 under Extreme Deformation. *Applied Physics Letters* **2023**, *122*, 211906.

572 (23) Lookman, T.; Balachandran, P. V.; Xue, D.; Yuan, R. Active Learning in Materials Science
573 with Emphasis on Adaptive Sampling Using Uncertainties for Targeted Design. *npj Comput*
574 *Mater* **2019**, *5*, 1–17.

575 (24) Prince, M. Does Active Learning Work? A Review of the Research. *Journal of Engineering*
576 *Education* **2004**, *93*, 223–231.

577 (25) Smith, J. S.; Nebgen, B.; Lubbers, N.; Isayev, O.; Roitberg, A. E. Less Is More: Sampling
578 Chemical Space with Active Learning. *The Journal of Chemical Physics* **2018**, *148*, 241733.

579 (26) Schmidt, J.; Marques, M. R. G.; Botti, S.; Marques, M. A. L. Recent Advances and Appli-
580 cations of Machine Learning in Solid-State Materials Science. *npj Comput Mater* **2019**, *5*,
581 1–36.

582 (27) Jorgensen, W. L.; Maxwell, D. S.; Tirado-Rives, J. Development and Testing of the OPLS
583 All-Atom Force Field on Conformational Energetics and Properties of Organic Liquids. *J.
584 Am. Chem. Soc.* **1996**, *118*, 11225–11236.

585 (28) Thompson, A. P.; Aktulga, H. M.; Berger, R.; Bolintineanu, D. S.; Brown, W. M.;
586 Crozier, P. S.; in 't Veld, P. J.; Kohlmeyer, A.; Moore, S. G.; Nguyen, T. D.; Shan, R.;
587 Stevens, M. J.; Tranchida, J.; Trott, C.; Plimpton, S. J. LAMMPS - a Flexible Simulation
588 Tool for Particle-Based Materials Modeling at the Atomic, Meso, and Continuum Scales.
589 *Comp. Phys. Comm.* **2022**, *271*, 108171.

590 (29) Grandbois, M.; Beyer, M.; Rief, M.; Clausen-Schaumann, H.; Gaub, H. E. How Strong Is a
591 Covalent Bond? *Science* **1999**, *283*, 1727–1730.

592 (30) Garcia, F. G.; Soares, B. G.; Pita, V. J. R. R.; Sánchez, R.; Rieumont, J. Mechanical Properties
593 of Epoxy Networks Based on DGEBA and Aliphatic Amines. *Journal of Applied Polymer
594 Science* **2007**, *106*, 2047–2055.

595 (31) Vashisth, A.; Ashraf, C.; Bakis, C. E.; van Duin, A. C. T. Effect of Chemical Structure
596 on Thermo-Mechanical Properties of Epoxy Polymers: Comparison of Accelerated ReaxFF
597 Simulations and Experiments. *Polymer* **2018**, *158*, 354–363.

598 (32) Bartók, A. P.; Kondor, R.; Csányi, G. On Representing Chemical Environments. *Phys. Rev. B*
599 **2013**, *87*, 184115.

600 (33) De, S.; Bartók, A. P.; Csányi, G.; Ceriotti, M. Comparing Molecules and Solids across Struc-
601 tural and Alchemical Space. *Phys. Chem. Chem. Phys.* **2016**, *18*, 13754–13769.

602 (34) Himanen, L.; Jäger, M. O. J.; Morooka, E. V.; Federici Canova, F.; Ranawat, Y. S.; Gao, D. Z.;
603 Rinke, P.; Foster, A. S. Dscribe: Library of Descriptors for Machine Learning in Materials
604 Science. *Computer Physics Communications* **2020**, *247*, 106949.

605 (35) Chang, C.-C.; Lin, C.-J. LIBSVM: A Library for Support Vector Machines. *ACM transac-*
606 *tions on intelligent systems and technology (TIST)* **2011**, *2*, 1–27.

607 (36) Boerner, T. J.; Deems, S.; Furlani, T. R.; Knuth, S. L.; Towns, J. *Practice and Experience in*
608 *Advanced Research Computing*; 2023; pp 173–176.

609 (37) Cohn, D. A.; Ghahramani, Z.; Jordan, M. I. Active Learning with Statistical Models. *Journal*
610 *of artificial intelligence research* **1996**, *4*, 129–145.

611 (38) Settles, B. Active Learning Literature Survey. **2009**,

612 (39) Settles, B. From Theories to Queries: Active Learning in Practice. Active Learning and Ex-
613 perimental Design Workshop In Conjunction with AISTATS 2010. 2011; pp 1–18.

614 (40) Bannwarth, C.; Ehlert, S.; Grimme, S. GFN2-xTB—An Accurate and Broadly Parametrized
615 Self-Consistent Tight-Binding Quantum Chemical Method with Multipole Electrostatics and
616 Density-Dependent Dispersion Contributions. *J. Chem. Theory Comput.* **2019**, *15*, 1652–
617 1671.

618 (41) Schohn, G.; Cohn, D. Less Is More: Active Learning with Support Vector Machines. ICML.
619 2000; p 6.

620 (42) Kremer, J.; Steenstrup Pedersen, K.; Igel, C. Active Learning with Support Vector Machines.
621 *WIREs Data Mining and Knowledge Discovery* **2014**, *4*, 313–326.

622 (43) Platt, J., et al. Probabilistic Outputs for Support Vector Machines and Comparisons to Regu-
623 larized Likelihood Methods. *Advances in large margin classifiers* **1999**, *10*, 61–74.

624 (44) Neese, F.; Wennmohs, F.; Becker, U.; Ripplinger, C. The ORCA Quantum Chemistry Program
625 Package. *J. Chem. Phys.* **2020**, *152*, 224108.

626 (45) Meng, Z.; Bessa, M. A.; Xia, W.; Kam Liu, W.; Keten, S. Predicting the Macroscopic Fracture
627 Energy of Epoxy Resins from Atomistic Molecular Simulations. *Macromolecules* **2016**, *49*,
628 9474–9483.

629 (46) Kubát, M.; Matwin, S. Addressing the Curse of Imbalanced Training Sets: One-sided Selec-
630 tion. International Conference on Machine Learning. 1997.

631 (47) Konrad, J.; Meißner, R. H.; Bitzek, E.; Zahn, D. A Molecular Simulation Approach to Bond
632 Reorganization in Epoxy Resins: From Curing to Deformation and Fracture. *ACS Polym. Au*
633 **2021**, *1*, 165–174.

634 (48) Moller, J. C.; Barr, S. A.; Schultz, E. J.; Breitzman, T. D.; Berry, R. J. Simulation of Fracture
635 Nucleation in Cross-Linked Polymer Networks. *JOM* **2013**, *65*, 147–167.

636 (49) Li, C.; Medvedev, G. A.; Lee, E.-W.; Kim, J.; Caruthers, J. M.; Strachan, A. Molecular
637 Dynamics Simulations and Experimental Studies of the Thermomechanical Response of an
638 Epoxy Thermoset Polymer. *Polymer* **2012**, *53*, 4222–4230.

639 (50) Li, C.; Strachan, A. Molecular Dynamics Predictions of Thermal and Mechanical Properties
640 of Thermoset Polymer EPON862/DETDA. *Polymer* **2011**, *52*, 2920–2928.

641 (51) Yoshimoto, K.; Jain, T. S.; Workum, K. V.; Nealey, P. F.; de Pablo, J. J. Mechanical Het-
642 erogeneities in Model Polymer Glasses at Small Length Scales. *Phys. Rev. Lett.* **2004**, *93*,
643 175501.

644 (52) Riggleman, R. A.; Lee, H.-N.; Ediger, M. D.; de Pablo, J. J. Free Volume and Finite-Size
645 Effects in a Polymer Glass under Stress. *Phys. Rev. Lett.* **2007**, *99*, 215501.

646 (53) Pink, E.; Campbell, J. D. The Low-Temperature Macro Deformation of an Epoxide Resin.
647 *Materials Science and Engineering* **1974**, *15*, 187–194.

648 (54) Mayr, A. E.; Cook, W. D.; Edward, G. H. Yielding Behaviour in Model Epoxy Thermosets
649 — I. Effect of Strain Rate and Composition. *Polymer* **1998**, *39*, 3719–3724.

650 (55) Fan, J.; Anastassiou, A.; Macosko, C. W.; Tadmor, E. B. Molecular Dynamics Predictions
651 of Thermomechanical Properties of an Epoxy Thermosetting Polymer. *Polymer* **2020**, *196*,
652 122477.

653 (56) Tamrakar, S.; Ganesh, R.; Sockalingam, S.; Haque, B. Z.; Gillespie, J. W. Experimental
654 Investigation of Strain Rate and Temperature Dependent Response of an Epoxy Resin Under-
655 going Large Deformation. *J. dynamic behavior mater.* **2018**, *4*, 114–128.

656 (57) Ediger, M. D.; Angell, C. A.; Nagel, S. R. Supercooled Liquids and Glasses. *J. Phys. Chem.*
657 **1996**, *100*, 13200–13212.

658 (58) Barrat, J.-L.; Baschnagel, J.; Lyulin, A. Molecular Dynamics Simulations of Glassy Poly-
659 mers. *Soft Matter* **2010**, *6*, 3430–3446.

660 (59) Yu, Z.; Liu, Q.; Szlufarska, I.; Wang, B. Structural Signatures for Thermodynamic Stability
661 in Vitreous Silica: Insight from Machine Learning and Molecular Dynamics Simulations.
662 *Phys. Rev. Materials* **2021**, *5*, 015602.

663 (60) Shokuhfar, A.; Arab, B. The Effect of Cross Linking Density on the Mechanical Properties
664 and Structure of the Epoxy Polymers: Molecular Dynamics Simulation. *J Mol Model* **2013**,
665 *19*, 3719–3731.

666 (61) van Duin, A. C. T.; Dasgupta, S.; Lorant, F.; Goddard, W. A. ReaxFF: A Reactive Force Field
667 for Hydrocarbons. *J. Phys. Chem. A* **2001**, *105*, 9396–9409.

668 (62) Liu, L.; Liu, Y.; Zybin, S. V.; Sun, H.; Goddard, W. A. I. ReaxFF-lg: Correction of the
669 ReaxFF Reactive Force Field for London Dispersion, with Applications to the Equations of
670 State for Energetic Materials. *J. Phys. Chem. A* **2011**, *115*, 11016–11022.

671 (63) Lin, S.; Zhao, X. Fracture of Polymer Networks with Diverse Topological Defects. *Phys. Rev. E* **2020**, *102*, 052503.

673 (64) Wu, X.; El-Awady, J. A. In *Integrated Computational Materials Engineering (ICME): Advancing Computational and Experimental Methods*; Ghosh, S., Woodward, C., Przybyla, C.,
674 Eds.; Springer International Publishing: Cham, 2020; pp 267–296.

675

676 (65) Littell, J. D.; Ruggeri, C. R.; Goldberg, R. K.; Roberts, G. D.; Arnold, W. A.; Binienda, W. K.
677 Measurement of Epoxy Resin Tension, Compression, and Shear Stress–Strain Curves over a
678 Wide Range of Strain Rates Using Small Test Specimens. *Journal of Aerospace Engineering*
679 **2008**, *21*, 162–173.

680 (66) Bukowski, C.; Zhang, T.; Riggelman, R. A.; Crosby, A. J. Load-Bearing Entanglements in
681 Polymer Glasses. *Science Advances* **2021**, *7*, eabg9763.

682 (67) Chen, J.-S.; Ober, C. K.; Poliks, M. D.; Zhang, Y.; Wiesner, U.; Cohen, C. Controlled Degrade-
683 ration of Epoxy Networks: Analysis of Crosslink Density and Glass Transition Temperature
684 Changes in Thermally Reworkable Thermosets. *Polymer* **2004**, *45*, 1939–1950.

685 (68) Zhao, S.; Abu-Omar, M. M. Renewable Epoxy Networks Derived from Lignin-Based
686 Monomers: Effect of Cross-Linking Density. *ACS Sustainable Chem. Eng.* **2016**, *4*, 6082–
687 6089.

688 (69) Schichtel, J. J.; Chattopadhyay, A. Modeling Thermoset Polymers Using an Improved Molec-
689 ular Dynamics Crosslinking Methodology. *Computational Materials Science* **2020**, *174*,
690 109469.

691 (70) Bay, R. K.; Zhang, T.; Shimomura, S.; Ilton, M.; Tanaka, K.; Riggelman, R. A.; Crosby, A. J.
692 Decoupling the Impact of Entanglements and Mobility on the Failure Properties of Ultrathin
693 Polymer Films. *Macromolecules* **2022**, *55*, 8505–8513.

694 (71) Wu, X.; Aramoon, A.; El-Awady, J. A. Hierarchical Multiscale Approach for Modeling the
695 Deformation and Failure of Epoxy-Based Polymer Matrix Composites. *J. Phys. Chem. B*
696 **2020**, *124*, 11928–11938.

697 (72) Boarino, A.; Charmillot, J.; Figueirêdo, M. B.; Le, T. T. H.; Carrara, N.; Klok, H.-A. Ductile,
698 High-Lignin-Content Thermoset Films and Coatings. *ACS Sustainable Chem. Eng.* **2023**, *11*,
699 16442–16452.